

Microstructure and Fracture Toughness of an Aluminum-Steel Impact Weld and Effect of Thermal Exposure



NOAH KOHLHORST, ANGSHUMAN KAPIL, ZHANGQI CHEN, ANUPAM VIVEK, TAESEON LEE, JI-CHENG ZHAO, and GLENN DAEHN

Welding of aluminum alloys to steel is increasingly important in manufacturing; however, the use of fusion welding is difficult because of disparate melting points and the possibility of intermetallic compound (IMC) formation. Here, an impact welding technique, vaporizing foil actuator welding, was utilized to produce solid-state joints between AA1100-O and 1018 mild steel. The relationship between weld processing conditions, microstructure, and mechanical properties was investigated. For this purpose, the welds were annealed between 300 °C and 600 °C and a combination of optical and scanning electron microscopy, along with image analysis was performed to characterize the weld microstructure and monitor IMC growth. Wedge testing was applied to understand the effect of annealing on the weld fracture toughness. A numerical model incorporating the Fick's laws of diffusion, grain boundary diffusion, and grain growth kinetics was also developed to simulate the IMC growth. The heterogeneity in the original microstructure caused persistent differences in IMC growth, as initial IMC seemed to increase nucleation and growth. Simulation results indicated short circuit diffusion to be the major contributor to IMC growth since it is consistently faster than experimental IMC growths compared with the computational results that used lattice diffusion only. Wedge testing reveals increased weld toughness for modest anneals of 300 °C, possibly due to homogeneity at the weld interface while avoiding IMC growth.

<https://doi.org/10.1007/s11661-021-06269-7>

© The Minerals, Metals & Materials Society and ASM International 2021

I. INTRODUCTION

WITH a greater need to address global emission concerns and reduce global carbon footprint, there have been renewed efforts to optimize welding processes and introduce multi-material combinations for a wide range of applications.^[1,2] Dissimilar welding of aluminum (Al) to steel is one of the most important of these applications; however, the product designers and manufacturers are largely constrained by the limitations of the

conventional welding technologies, as they limit the quality and properties of the dissimilar joint.^[2,3] Al and steel find applications in transportation,^[1-4] aerospace,^[2-4] structural, and shipbuilding.^[3,5] Al alloys are inexpensive, light weight, have high corrosion resistance, and can demonstrate high strength under proper processing conditions.^[6,7] Steels are used heavily in structural applications where high strength and toughness are desired.^[8] Joining these disparate alloys allows access to the different desirable properties of each material class; however, the strength of the Al alloy—steel weld is greatly influenced by the type of welding process employed.^[4]

Dissimilar Al-steel joining through conventional fusion welding techniques like resistance spot welding (RSW) is difficult due to the formation of brittle intermetallic compounds (IMC's) and has been widely discussed in the literature.^[9-12] Mechanical fastening techniques like self-piercing riveting (SPR), flow drilling screws (FDS), etc. have been utilized for Al-steel joining, but there are limitations on stack-up feasibility, and the use of an externally exposed joining element increases the susceptibility of the joint to galvanic corrosion.^[13] Industries have been employing solid-state welding

NOAH KOHLHORST is with the Department of Materials Science and Engineering, The Ohio State University, Columbus, OH 43210 and also with the Materials Science and Technology Division, Alloying Behavior and Design Group, Oak Ridge National Laboratory (ORNL), Oak Ridge, TN, 37831-6285. Contact e-mail: nkohlhorst6@gmail.com ANGSHUMAN KAPIL, ZHANGQI CHEN, ANUPAM VIVEK, and GLENN DAEHN are with the Department of Materials Science and Engineering, The Ohio State University. TAESEON LEE is with the Department of Mechanical Engineering, Incheon National University, Incheon, 22012 South Korea. JI-CHENG ZHAO is with the Department of Materials Science and Engineering, University of Maryland, College Park, MD 20742.

Manuscript submitted September 5, 2020, accepted March 25, 2021.
Article published online April 19, 2021

techniques such as friction stir welding (FSW), ultrasonic welding (USW), roll bonding, and impact welding as viable substitutes to traditional welding techniques like fusion welding or mechanical fastening techniques on a small scale.^[14] The present study utilizes the vaporizing foil actuator welding (VFAW), an impact welding technique developed at the Impulse Manufacturing Laboratory at The Ohio State University (OSU), to produce nominally solid-state dissimilar Al-steel joints. The VFAW process causes high-speed collision (typically hundreds of m/s) of flyer and target sheets to generate a joint with negligible melting and with little to no presence of a heat-affected zone (HAZ), providing opportunities to join a wide array of dissimilar materials.^[15] The high pressures required to drive the metal sheets are provided by the rapid vaporization of a metallic foil actuator.

Al-rich brittle IMC's (FeAl_3 , Fe_2Al_5) are frequently formed at the interface of the dissimilar Al-steel welds, irrespective of the welding process employed.^[16] The growth and thickness of the IMC layer, however, depends on the heat input to the weld interface during the joining process as well as on the post-weld heat treatment (annealing).^[16] Post-weld annealing treatment is useful for reducing residual stresses, promoting metallurgical bonding at the weld interface and its vicinity, and improving formability for secondary processes like rolling or deep drawing.^[3,17] An understanding of the effects of thermal exposure is also desirable as many functional parts used in industry are made up of welds that can undergo many subsequent thermal processing steps. The IMC's generally differ greatly in properties from the base metals and, thus, play a crucial role in determining the overall joint performance. There is a significant relationship between the thickness of the IMC layer and the strength of the dissimilar Al-steel joint.^[18] Therefore, in order to properly design the properties of the dissimilar joints, it is important to have an accurate understanding of the relationship of IMC growth, the joint strength, and the welding process. Understanding the trend of weld strength with IMC thickness is important as it provides annealing guidelines to maximize the formability of a part consisting of Al-steel dissimilar weld while minimizing the reduction in weld strength.

Several experimental studies have been conducted to measure the growth of IMC layers at the interface using various welding processes^[1,3,17,19,20] as well as diffusion bonding to make diffusion couples^[21,22] with different heat treatments. In one study,^[21] diffusion bonded couples of Al-Fe were heat treated between 550 °C and 640 °C with only Fe_2Al_5 forming at the interface.^[21] At this temperature range, FeAl_2 , BCC_B2, and FeAl_3 are thermodynamically stable phases, but have very slow formation rates such that these could not form into observable intermetallic layers at the interface in the annealing times conducted in their study.^[21] Heat treating the friction stir welds between 350 °C and 450 °C resulted in the formation of FeAl_3 and Fe_2Al_5 at the interface.^[3] It was observed that Fe_2Al_5 made up most of the IMC layer and the growth rate of the IMC layers was not governed by the parabolic diffusion

law.^[3] The as-welded friction stir welds contained both high stored energy and the presence of IMC's at the weld interface caused the growth of IMC's to deviate from the parabolic diffusion law.^[3] To study the influence of the IMC growth (aided by annealing) on the joints mechanical properties in Al-steel welds, several authors have investigated both solid-state joining processes^[23–25] and fusion-based processes.^[26,27] The general observation was that by increasing IMC thickness with annealing treatment, the Al-steel joint strength and toughness decreased, and the failure of the samples occurred in the interface. Several studies also involved development of simulation techniques to calculate the IMC growth at the interface of an Al-Fe diffusion couple with respect to annealing temperature.^[19,21,28,29] The relatively discrete and low-temperature bonding of VFAW offers a unique opportunity to create a fairly defect-free initial interface that can be subjected to further thermal exposure.

Studies relating the weld strength to IMC growth for Al-steel welds have reported a range of critical IMC thickness values for a variety of processes. Qiu *et al.*^[12] and Miyamoto *et al.*^[30] reported significant drop in cross-tension strength values for IMC growth beyond 1.5 and 2 μm , respectively, for RSW. Chen *et al.*^[31] measured the fracture toughness of Al-Fe resistance spots welds with respect to Fe_2Al_5 growth at the weld interface and reported that an IMC growth larger than 3 μm caused a drastic reduction in weld fracture toughness. Hatano *et al.*^[16] measured the tensile strength of Al-Fe dissimilar friction stir welds as a function of post-welding heat treatments. Their results showed that the fracture position changed from the base material on the Al side to inside the IMC layer and the tensile strength dropped by a factor of three when the IMC layer thickness increased from 0.5 to 2–5 μm . Springer *et al.*^[18] found that the tensile strengths for friction stir welded Al-steel joints dropped significantly and failure mode switched to interfacial when IMC growth exceeded 7 μm . Similar results have been reported for other Al-steel friction stir lap welding studies where drastic drop in joint strengths was seen when IMC thickness exceeded a certain thickness (0.5 μm ,^[32] 2.6 μm ^[33] and 5 μm ^[34]). Yang *et al.*^[35] obtained relatively high weld strengths for cold metal transfer Al-steel welds when the IMC thickness was controlled below 10 μm .

VFAW, due to the inherent nature of the process, produces a large amount of plasticity at the interface. Annealing these welds can soften the bonded region and possibly heal small existing voids, but at a cost of IMC formation which can be detrimental to the mechanical properties of the weld. Control of the experimental parameters can minimize the extent of melting at the interface, limiting the formation of IMC's. In this study, the growth of IMC in Al-steel impact welds through different heat treatment conditions was addressed with the application of first principles calculations using the finite difference method (FDM). The developed model explicitly considered grain boundary and lattice diffusion pathways. VFAW welds between AA1100-O and 1018 mild steel were prepared and heat treated with

different annealing conditions to generate various thicknesses of IMC layers at the weld interface. These results were used to validate the computational work. To the authors' best knowledge, in most of the studies involving Al-steel welding, the mechanical property evaluation as a function of annealing has been limited to either lap-shear or cross-tension testing. The use of a wedge to measure the fracture toughness of brazed joints has been developed by Philips *et al.*^[36] This technique has been adopted and modified in this study to handle the geometry of Al-steel VFAW welds to generate interfacial failures in the welds for the purpose of estimating the fracture toughness of the joints. Optical microscopy (OM), scanning electron microscopy (SEM), and image analysis were carried out to characterize the weld microstructure and evaluate the growth of IMCs with respect to the different annealing conditions.

II. MATERIALS AND METHODS

A. Materials

2-mm-thick 1018 mild steel cut into 76.2×76.2 mm squares and 3-mm-thick AA1100-O cut into 76.2×50.8 mm rectangular sheets were used in the present study. One side of the cut steel sheet was roughly ground using sandpaper and then cleaned using acetone prior to welding to remove any surface contaminants.

B. Welding Setup

A schematic of the VFAW experimental assembly is illustrated in Figure 1(a). A 76- μm -thick AA1100 foil with dimensions illustrated in Figure 1(b) was placed on the bottom half of a rigid steel fixture. The Al foil was encased in a plastic sleeve and was insulated from the bottom fixture and the workpiece through the use of polyester tape. Lines were marked on the plastic sleeve to guide proper placement of the proceeding components to ensure the setup between every experiment was approximately the same. The Al sheet, chosen as the flyer sheet in this study, was placed on top of the insulated Al foil. Two 1.60 mm standoffs spaced 31.7 mm apart were placed on top of the Al flyer as shown in the Figure 1(a). The steel target sheet was placed over the Al flyer containing the standoffs. A backing block followed by the top of the fixture were placed on top of the target sheet. The fixture was tightened with bolts to keep everything secured. The fixture assembly was connected to the terminals of a Maxwell Magneform capacitor bank capable of discharging up to 16 kJ.^[4] A discharge energy of 12 kJ was used for every experiment in this work. Adequate experiments were conducted to yield at least three welds per annealing condition. Figure 1(c) depicts a schematic representation of the workpiece assembly post vaporization of the foil and impact of the mating members. It is to be noted that in impact welds the center of the weld remains unbonded and metallurgical bonds are only achieved starting at a certain distance from the center. This is a consequence of the locally evolving collision speed and angle. The

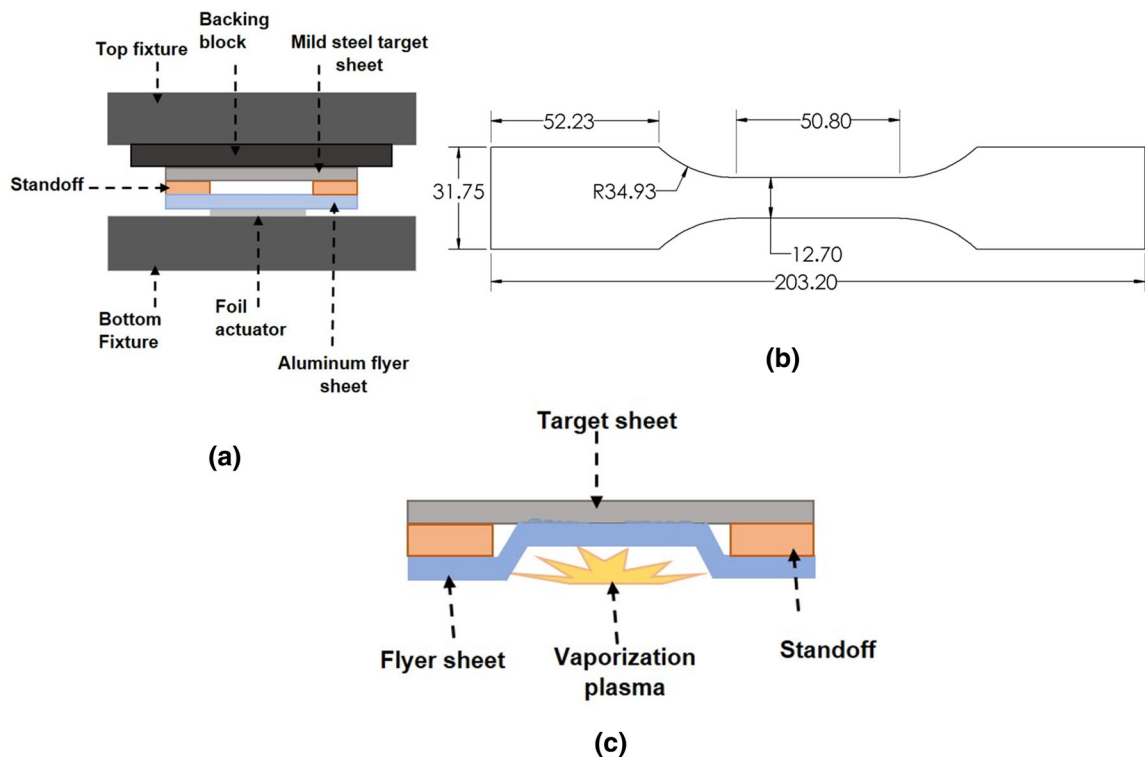


Fig. 1—(a) VFAW experimental setup, (b) Al foil dimensions, and (c) schematic of VFAW weld post foil vaporization and impact of flyer and target sheets (all dimensions are in mm).

center of the weld has normal impact which does not produce any impact weld.

C. Thermal Exposure and Characterization

Figure 2(a) presents an overall view of the welded sample, whereas Figure 2(b) shows the location of the cuts for preparing the samples for heat treatment and wedge testing. Each prepared weld was cut into 20 mm wide strips using a circular abrasive saw. The black dashed lines in Figure 2(b) show the location of the cuts. Samples for microscopy employed the same cutting method, except the 20 mm strips were cut into two smaller pieces (10 mm wide strips) and the steel bottom were cut off. These pieces were then mounted, ground and polished down to 1 μm diamond paste for OM and SEM.

For mechanical testing, batches of three VFAW cut samples were heat treated in a vacuum furnace at 300 °C, 400 °C, 450 °C, 500 °C, 525 °C, 550 °C, and 600 °C. The heat treatment time was constant at 140 minutes for all the cases. The choice of annealing conditions was guided by References 3, 21. For OM, small overlapping images were taken across the entire welded region prior to and after heat treatment. After the OM images were stitched together for each sample prior to heat treatment, the samples were broken out of the mount, then heat treated following the annealing conditions listed above. Once the samples were annealed, they were remounted, ground and polished down to 1 μm diamond paste for OM and SEM analysis. Note the surfaces for each mounted annealed sample was ground down at least 1 mm prior to the final polishing step to avoid capturing any surface diffusion effects on the microstructure from OM analysis posing the risk of generating unreliable IMC thickness measurements. OM images were again taken across the annealed welds to generate montages.

The as-welded and heat-treated Al-steel VFAW montages were then processed in the software ImageJ to calculate the average increase in IMC thickness across the length span of each weld. As-welded and heat-treated samples that were prepared for SEM and energy-dispersive spectroscopy (EDS) analysis followed

the same process as the samples prepared for OM except no as-welded images were taken. A Thermofisher Apreo FEG instrument was used for SEM and EDS analysis.

D. Mechanical Testing

A wedge testing technique was employed to measure the weld fracture toughness. The wedge test has a long history in measuring the crack growth resistance at similar and dissimilar material interfaces.^[36,37] In this case it was adapted for use without careful regard to standards, therefore it should provide relative measures of toughness, no attempt is made to quantify the crack growth resistance. In this technique, a hardened S7 tool steel wedge with a point angle of 28 deg was forced between two fixed welded sheets at a steady speed of 3 mm/min. This produces a crack opening force between the two welded materials to peel away eventually resulting in interfacial failure when the peeling force exceeded the strength of the weld. If the interface is tougher than the parent materials, the wedge may cut through the weaker of the two base metals, which in this case is the aluminum. An MTS Criterion Model 43 was used for the wedge testing. The wedge testing set up and the wedge dimensions are depicted in Figures 3(a) and (b), respectively.

The steel side fracture surface of a couple of peeled samples were investigated using SEM to test the validity of the wedge testing method and ascertain a successful test, as explained in Section III-A. Both secondary electron (SE) and backscattered electron (BSE) images were taken. EDS maps were also taken on each surface to check for material transfer during peeling.

E. Computational Modeling of Interdiffusion

Pydiffusion is an open-source python library designed to efficiently simulate various types of 1D binary or ternary diffusion problems.^[38] A method within Pydiffusion has been developed to construct concentration profiles of binary multi-phase systems governed by temperature-dependent interdiffusion data and time.^[38] Based on pre-constructed 1D grids, the simulation applies the finite difference method (FDM) to

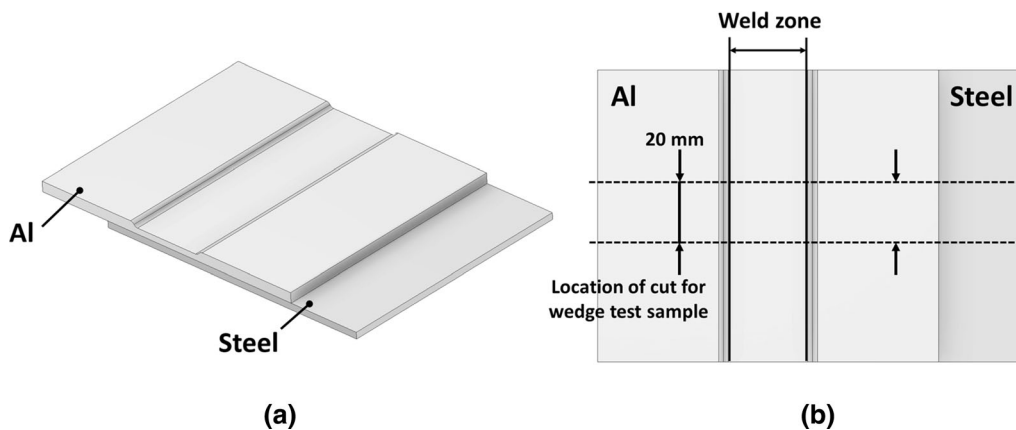


Fig. 2—(a) Overall view of the Al-Steel weld, and (b) illustration of preparation of VFAW samples for annealing and wedge testing.

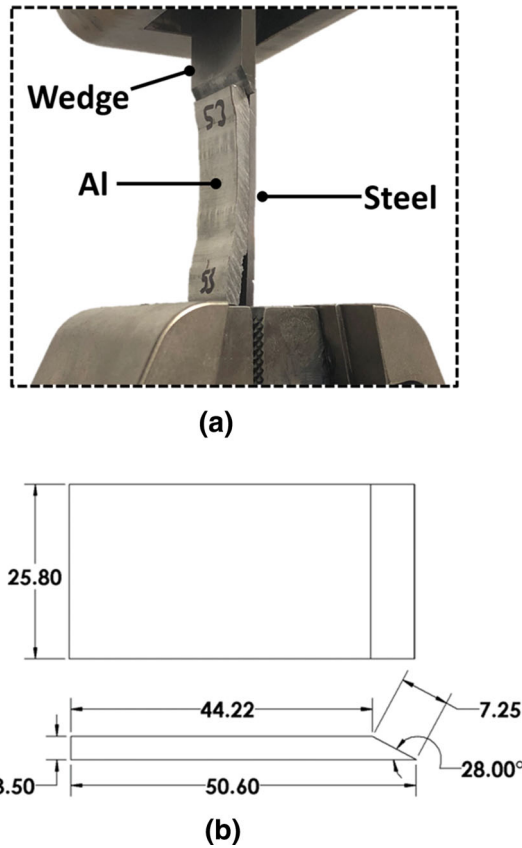


Fig. 3—(a) Wedge testing set up and (b) Geometry and dimensions (mm) of the wedge.

numerically solve the diffusion problems using Fick's two laws of solid-state diffusion (Eq. [1]).

$$J = -\tilde{D} \frac{\partial c}{\partial x} \text{ and } \frac{\partial C}{\partial t} = \frac{\partial}{\partial x} \left(-\tilde{D} * \frac{\partial c}{\partial x} \right) \quad [1]$$

where, \tilde{D} is the interdiffusion coefficient, $\frac{\partial c}{\partial x}$ is the concentration gradient, J is the diffusion flux, and $\frac{\partial C}{\partial t}$ is derivative of diffusion flux. This is applied to within a given phase.^[38] To account for a system containing multiple phases, the position of the interface between two adjacent phases is calculated by Eq. [2].

$$\frac{dx}{dt} = \frac{J_\alpha - J_\beta}{C_\alpha - C_\beta} \quad [2]$$

where J_α , J_β , C_α and C_β are the atomic fluxes and compositions evaluated at the interface in phases α and β , respectively.^[38] The interfaces in the simulation are defined by a composition range set with boundaries. The composition at the boundaries corresponds to solubility limits C_α and C_β of given phases. We applied the sharp interface model to all simulation systems in this study. The sharp interface model permits the movement of the interfaces controlled by Eq. [2]. In Pydiffusion, the interfaces are not restricted by the grid points from the FDM, meaning that they can pass through grid points without rearranging them. If one interface passes through a grid point defined by its position,

composition, and phase, the phase for that grid point will be re-assigned.^[38]

The Al-Fe binary diffusion couple with a total of four phases are introduced in this study. These phases comprised of two solid-solution phases (FCC-Al and Al-Fe BCC) and two IMC's (FeAl₃ and Fe₂Al₅). 200 grid points non-linearly spaced were meshed in the setup, in which smaller spacings was used nearby the phase interfaces. The interdiffusion coefficients data for this simulation were developed using experimental lattice interdiffusion data from several external sources.^[21,29,39,40] The impurity diffusion of Al in Fe and Fe in Al were collected from Reference 39 experimental interdiffusion coefficients data in the Al-Fe BCC phase from 1 at. pct Fe to 51 at. pct Fe were collected from References 29, 40. The interdiffusion coefficients of the Fe₂Al₅ IMC was collected from References 21 where the authors quantitatively evaluated the interdiffusion in Fe₂Al₅ at a temperature range between 550 °C and 640 °C. The pre-exponential factors (D_0) and activation energy (Q) for diffusion were calculated from all the collected data. Since the interdiffusion data from two sources were used in the Al-Fe BCC phase, the average D_0 and Q were computed. No reported interdiffusion data in the FeAl₃ phase were found. However, FeAl₃ phase has a very similar composition and melting point to Fe₂Al₅, so we can apply the same interdiffusion coefficients in both phases. The initial setup of the Al-Fe diffusion problem and a profile of the lattice interdiffusion coefficients in the Al-Fe system at 550 °C is illustrated in Figures 4(a) and (b).

Since VFAW generates highly deformed grains with high dislocation densities and recrystallized grains of sizes less than 1 μm on the Al side at the weld interface,^[41] running the simulation with lattice diffusion coefficients does not represent the microstructure outcome of annealed VFAW welds very well. This conclusion was reached after attempting to run the simulation using the lattice diffusion coefficients and observing large discrepancies between the calculated and experimental results as explained in detail in Section III-C. The simulation was therefore modified to include short circuit or grain boundary diffusion. This is accomplished by calculating the effective diffusion coefficient (D_{eff}) as below:

$$D_{\text{eff}} = (1 - f) * D_L + f * D_{\text{GB}} \quad [3]$$

where, f is the volume fraction of grain boundary per unit volume, D_L is the lattice diffusion coefficient, and D_{GB} is the grain boundary diffusion coefficient.^[29] One thing to note is that the effective diffusion equations in the Al-FCC and the Al-Fe BCC solid-solution phases does not strongly influence the growth of the IMC's. The effective diffusion terms and equations for these phases can be found in Tables I and II.

Following the effective diffusion equation (Eq. [3]), f is strongly dependent on the grain size which continuously changes during thermal exposure. The grain shapes were taken to be cubes to simplify the mathematical relation between grain size and grain boundary volume fraction. With this simplification, the number of grain boundaries

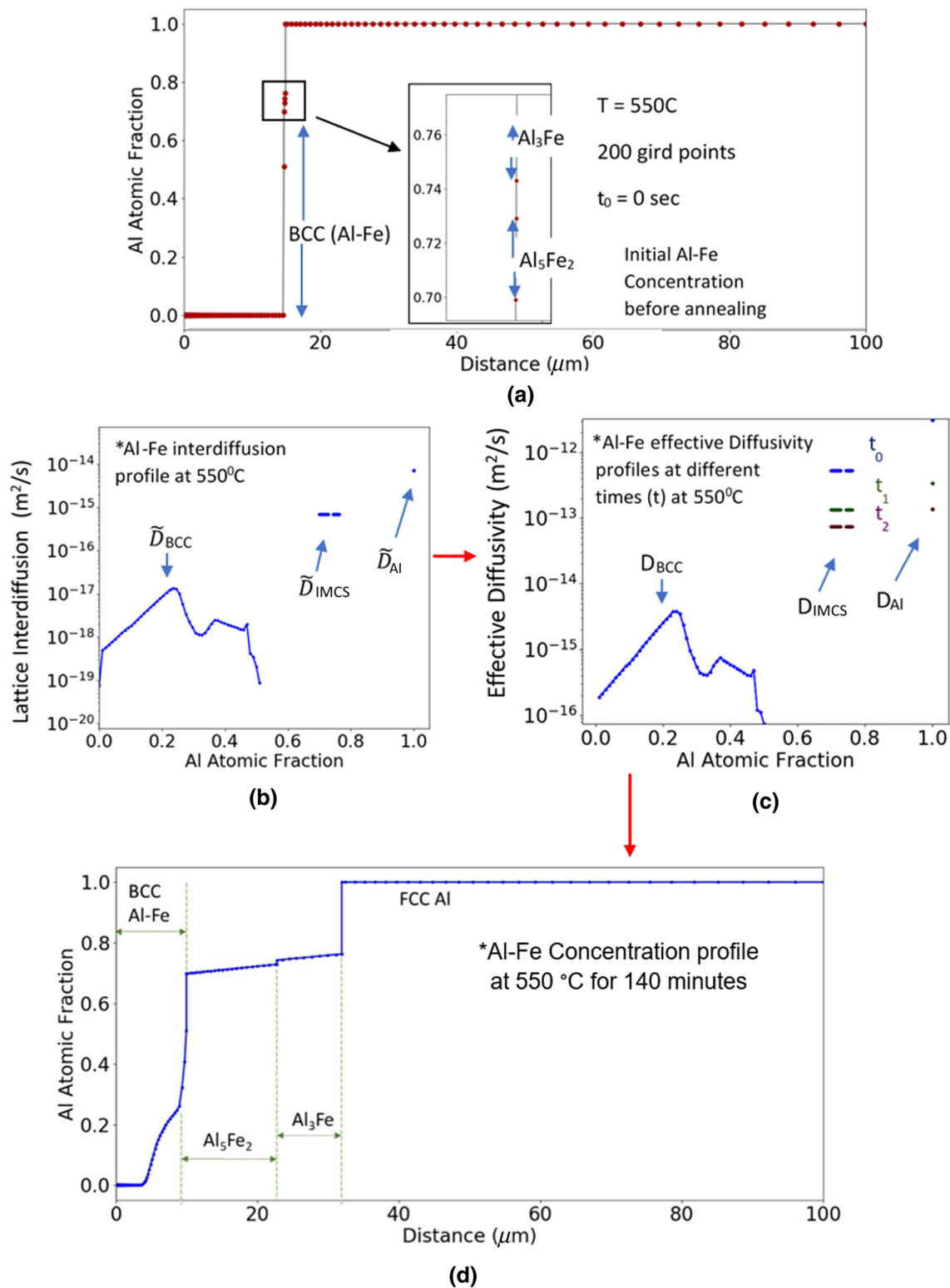


Fig. 4—(a) Initial setup of Al-Fe diffusion simulation in Pydiffusion, (b) lattice interdiffusion coefficients profile of labeled phases in the Al-Fe system using experimental data from Ref. [29], [39], [40], (c) profiles of effective interdiffusion coefficients of each marked phase of the Al-Fe system calculated after computational times of $t_0 = 0 \text{ min}$, $t_1 = 30 \text{ min}$, and $t_2 = 140 \text{ minutes}$ using experimental data from Ref. [20], [42–45] and (d) concentration profile of Pydiffusion simulation result.^[38]

per unit volume is $N_{\text{GB}} = 3n^3$ for large n , where n is the number of grains per unit length. Herzig *et al.* define the grain boundary volume fraction as $f = q^*\delta/d$ for

parallel grain in 2D.^[42] In this equation, d is the spacing between parallel grains and q defines the grain shape.^[42] In the current work, the volume fraction of grain

Table I. Collected Input Variables of Lattice Diffusion (D_L) and Grain Boundary Diffusion (D_{gb}) Functions With Temperature (T) at Different Atomic Compositions of Al Used in the Simulation

Al (At. Pct)	Phase	D_L (T)	D_{gb} (933K)	D_{gb} (T)
0	BCC	$1.80 \cdot 10^{-4} \cdot e^{-29113/T}$	$3.27 \cdot 10^4 \cdot D_L$	$\left(10^{(\log(D_{L(933K)})) + 0.5 \left(\log \left(\frac{D_L(T)}{D_{L(933K)}} \right) \right)} \right) \cdot \frac{D_{gb(933K)}}{D_{L(933K)}}$
5	BCC (solid solution)	$6.40 \cdot 10^{-4} \cdot e^{-28158/T}$	$3.23 \cdot 10^4 \cdot D_L$	
10		$6.56 \cdot 10^{-4} \cdot e^{-27611/T}$	$3.18 \cdot 10^4 \cdot D_L$	
15		$5.05 \cdot 10^{-4} \cdot e^{-26727/T}$	$3.13 \cdot 10^4 \cdot D_L$	
20		$4.61 \cdot 10^{-4} \cdot e^{-26016/T}$	$3.03 \cdot 10^4 \cdot D_L$	
25		$8.06 \cdot 10^{-4} \cdot e^{-26190/T}$	$2.92 \cdot 10^4 \cdot D_L$	
30		$1.71 \cdot 10^{-2} \cdot e^{-30455/T}$	$2.78 \cdot 10^4 \cdot D_L$	
35		$5.31 \cdot 10^{-3} \cdot e^{-29342/T}$	$2.61 \cdot 10^4 \cdot D_L$	
40		$3.31 \cdot 10^{-3} \cdot e^{-28821/T}$	$2.43 \cdot 10^4 \cdot D_L$	
45		$3.30 \cdot 10^{-3} \cdot e^{-29071/T}$	$2.24 \cdot 10^4 \cdot D_L$	
51		$6.18 \cdot e^{-37616/T}$	$1.96 \cdot 10^4 \cdot D_L$	
70-73	Al ₅ Fe ₂	$234 \cdot e^{-33197/T}$	$4.61 \cdot 10^3 \cdot D_L$	
74-76	Al ₃ Fe	$234 \cdot e^{-33197/T}$	$4.61 \cdot 10^3 \cdot D_L$	
100	Al (FCC)	$0.77 \cdot e^{-26581/T}$	$4.26 \cdot 10^3 \cdot D_L$	

Table II. Input Variables of Collected Grain Boundary Volume Fraction Equations ($f_{(T,\delta,t)}$) With Respect to Temperature (T), Grain Boundary Width (δ), and Time (t) of Each Phase in the Simulation

Phase	$f_{(T,\delta,t)}$	$D_{eff}(T,\delta,t)$
Fe-Al ₄₉ Fe ₅₁ (BCC)	$\frac{3 \cdot \delta}{2 \cdot 10^{-6}}$	$(1 - f_{(T,\delta,t)}) \cdot D_L + f_{(T,\delta,t)} \cdot D_{GB}$
Al ₅ Fe ₂	$\frac{3 \cdot \delta}{\left(g_d^0 + 2.71 \cdot 10^{-6} \cdot e^{-\frac{25980}{T} \cdot t} \right)^{0.4}}$	
Al ₃ Fe	$\frac{3 \cdot \delta}{\left(g_d^0 + 2.71 \cdot 10^{-6} \cdot e^{-\frac{25980}{T} \cdot t} \right)^{0.4}}$	
Al (FCC)	$\frac{3 \cdot \delta}{\left(g_d^0 + 3.34 \cdot 10^{11} \cdot e^{-\frac{46472}{T} \cdot t} \right)^{-0.0055 \cdot T + 6.1405}}$	

boundaries is defined by cube grains in 3D modifying the equation to $f = 3 \cdot \delta / g_d$ where the grain spacing d is replaced with the grain size (g_d) and q is replaced with 3., [The variable g_d in Al and Al-rich intermetallics were extracted from multiple experimental studies.^[20,42,43]

Following the well-known parabolic equation of grain growth discussed in Reference 20, the grain growth coefficients of the FeAl₃ and Fe₂Al₅ IMC's were extracted from the reported results from Reference 19. These results were used to produce grain growth equations in each phase. Grain growth equations for the Al-FCC was produced from the results of References 42, 43. Since the maximum heat treatment conducted in this study was 600 °C, it was assumed that grain growth is negligible in the Al-Fe BCC phase due to sluggish diffusion. The grain growth equations were used to create grain boundary volume fraction (f) equations with respect to temperature, grain boundary width, and time as reported for each phase and is presented in Table II.

No grain boundary diffusion has been reported in the Al-rich IMC's; however, two authors,^[44,45] reported Arrhenius parameters for grain boundary diffusion in Fe₃Al using the serial sectioning technique. An assumption was made that D_{gb}/D_L with the same temperature ratio T/T_m between Al-rich IMC's and the composition of Fe₃Al is approximately the same. That means for

example D_{gb}/D_L in the Fe₃Al compound at 50 pct the melting point of the composition of Fe₃Al is equal in magnitude to D_{gb}/D_L in the Fe₂Al₅ compound at 50 pct the melting temperatures of Fe₂Al₅. From this, D_{gb}/D_L was calculated at the aluminum melting temperature (933 K). Herzig *et al.*^[42] reported an Arrhenius plot comparing D_{gb} and D_L with T_m/T . D_{gb}/D_L was calculated for each phase at 933 K and the Arrhenius plot was used to determine D_{gb}/D_L as a function of temperature and composition in the Al-Fe system. The grain boundary diffusion values and equations for each IMC's and solid-solution phases are listed in Table I, whereas the effective diffusion equations for every phase in the Al-Fe system are reported in Table II.

An example plot of effective diffusion profiles calculated at 550 °C for three different times, $t_0 = 0$ minutes, $t_1 = 30$ minutes, and $t_2 = 140$ minutes is illustrated in Figure 4(c). The effective diffusion with respect to composition of Al in the Al-Fe system was calculated from Eq. [3]. The variables D_L , D_{GB} , and f in Eq. [3] were calculated using the equations found in Tables I and II at 550 °C. The reason why the effective diffusion coefficients for the Al-rich phases were plotted at different annealing times in Figure 4(c) is because the grain boundary volume fraction influenced by grain growth changes with short annealing times at or below 140 minutes at 550 °C. This means that the effective

diffusion in the Al-rich phases is sensitive to the annealing time at that temperature. Since the Al-Fe BCC phase has a much higher melting temperature, the grain growth kinetics are expected to be sluggish at 550 °C resulting in a negligible change in the grain boundary volume fraction for any annealing time at or below 140 minutes. This means that the effective diffusion in that phase is expected to be insensitive to annealing time at 550 °C which is why only one effective diffusion profile for that phase is observed in Figure 4(c). The initial grain size was taken to be 0.1 μm for the Al-rich IMC phases. 0.1 and 2 μm was chosen for the Al-FCC and Al-Fe BCC solid-solution phases, respectively. The choice of initial grain sizes for the solid-solution phases is not very critical to the growth of IMC since the growth of the IMC is not strongly dependent by the magnitude of diffusion in those phases. Figure 4(d) illustrates a pydiffusion simulated concentration profile using the simulation setup.

The total IMC thickness is calculated as the sum of the thicknesses of FeAl_3 and Fe_2Al_5 phases. The entire simulation was repeated by varying the annealing temperatures incrementally from 300 °C to 600 °C. The simulation was also repeated by varying δ and initial grain size (g_d^0) of the Al-rich IMC phases as displayed in Table I. Similar to the Al-Fe BCC phase, changing g_d^0 in the pure Al phase has very minimal effect on the IMC growth outcome in the simulation, so a constant was given to that term.

III. RESULTS AND DISCUSSION

A. Weld Mechanical Properties

Figure 5 illustrates a representative force vs wedge displacement plot of a VFAW weld annealed at 450 °C for 140 minutes subjected to wedge testing. The measured curve ranges from a zero displacement, representing the start of the test when the wedge was a distance above the top weld to a maximum displacement when the wedge passes through the bottom weld. The two peaks on the curve are maximum forces before interfacial failure of the strongest parts of the top and bottom welds occur. A sudden drop in force illustrated by the nearly vertical lines to the right of the peaks in Figure 5

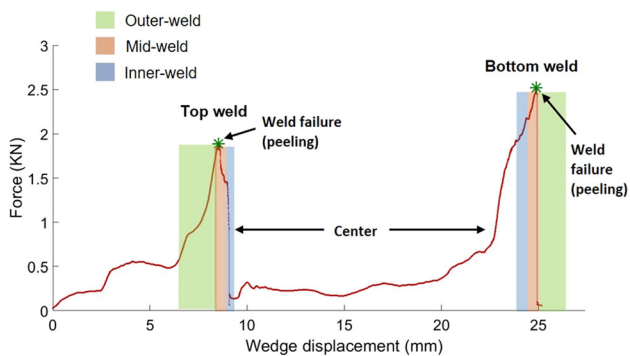
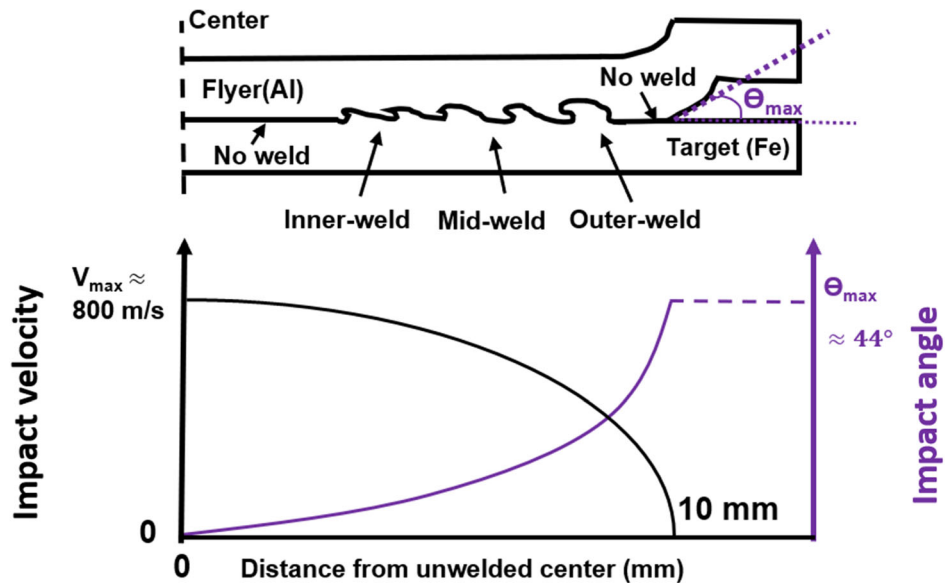


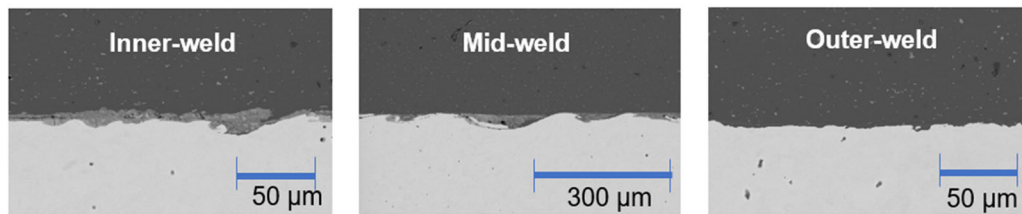
Fig. 5—Force vs wedge displacement curve from wedge test on a welded sample annealed at 450 °C for 140 min.

occur after each weld fails. The flatter curves before the peaks in Figure 5 are produced by the force of the wedge only bending the aluminum sheet away as the wedge approaches the welds. The colored shadings on the plot represent the different regions in each weld. These regions are illustrated and discussed in detail in Figure 6(a). Note that these shadings are only approximate and the distinctions between the weld zones are somewhat arbitrary, but this does capture the strongest part of the weld being in the central region where there may be some IMC formation, but those zones are discontinuous. It can be observed that the peaks on the force vs. wedge displacement curve corresponding to both the top and bottom welds are situated between the outer-weld and mid-weld regions. The outer-weld and outer portion of the mid-weld section contain the peaks on each curve as expected, since these regions have highest metallic bonding, and high deformation with the least amount of melting. A shoulder is observed between the peak and near vertical drop of the curve corresponding to the top weld. This shoulder is likely caused by the crack propagating through the weld slowly, resulting in sections of the weld to fail at different times. This outcome is also observed in the bottom weld where small fluctuations are seen on the force vs wedge displacement curve to the left of the peak.

Figure 7 represents box plots of weld fracture toughness of wedge-tested VFAW welds with respect to annealing temperatures. The weld fracture toughness values were calculated by dividing the maximum load to peel each VFAW weld (as seen in Figure 5) by the weld length. The box plots capture the spread of maximum weld peel strength. Figure 7 also shows a secondary plot (green diamond markers) capturing the IMC growth trend of VFAW welds with respect to annealing temperatures. Note that the green dotted line connecting the diamond markers is not a trend line and is used to enhance visual clarity of the data. Table III contains all the wedge test and IMC growth data with respect to annealing condition, and additional information with regard to the number of wedge tests conducted for each annealing condition and the type of failure modes observed. In Figure 7 each box captures multiple tests for the same annealing condition with the width of the box defining the number of tests. The top edge of the box represents the 3rd quartile, the red horizontal line represents the median, and the bottom edge of the box represents the 1st quartile of the data. The overall trend shows that the fracture toughness with annealing temperature increases up to 300 °C, then a reduction in toughness is observed up to 450 °C, followed by a slight increase in toughness up to 500 °C, then lastly it drops with annealing temperature exceeding 500 °C. While IMC thickness continued to increase beyond 300 °C, thermal exposure does not promote significant IMC growth and modest anneals at 300 °C in fact increased the bond toughness significantly (the median weld fracture toughness nearly doubled compared to the as-welded samples). This could be attributed to almost no observable IMC growth at this temperature. This is observed in Figure 8 which shows micrographs taken from three different regions for VFAW welds annealed



(a)



(b)

Fig. 6—(a) Schematics depicting (top) the evolution of impact velocity and impact angle with respect to the position along the weld interface and (bottom) the cross-section view of a VFAW weld between the Al flyer and steel target with each region labeled, and (b) micrographs depicting different regions of the Al-Fe VFAW weld in the as-welded condition (θ_{\max} has been measured experimentally).

at different temperatures ranging from 300 °C to 600 °C. Another likely reason for this is that modest anneals helped remove detrimental defects like voids at the weld interface without simultaneously growing IMC's. Although the lowest temperature heat treatment (300 °C) is not sufficient for any large-scale bulk diffusion, the newly formed interfaces have very high defect densities and may contain very thin oxide inclusions or high aspect ratio cracks. This modest temperature may be sufficient to coarsen small or high aspect ratio oxides, sinter together small asperities or relieve deleterious internal stresses. These processes may have activation energies much less than that for bulk diffusion. The reduction in fracture toughness as observed at and above 400 °C is associated with the formation of IMCs. Even at 400 °C where there are only a few microns of average IMC growth, the fracture toughness drops significantly. This suggests that the maximum toughness of these welds can be achieved with the choice of annealing temperature that maximizes the reduction of residual stresses at the weld interface while simultaneously preventing the growth of any IMCs, since even a small amount of IMC growth appears to be

deleterious to the weld strength. The failure mode for these samples are almost always base material cutting which differs from the failure mode of all other tested samples. However, as the IMC layer grows with increase of annealing temperature, even to only a few microns, the bond toughness decreases markedly. The majority of the weld fracture toughness is retained for IMC growths less than 10 μm , whereas as the IMC thickness grew beyond about 10 μm there was a rapid fall in fracture toughness.

This difference between the IMC growth to cause critical reduction in weld strength between this work and the previous works^[12,16,18–35] as mentioned in the Introduction section is likely due to the difference in the welding techniques and the testing methods employed. Note that there is no specific critical IMC thickness reported for Al-steel welding and all the reported value ranges between 1 and 10 μm . This is attributed to the fact that the IMC thickness is a function of several parameters including material composition, the brittleness of the IMC and its continuity as well as loading condition. In the previous works although the growth of the IMC's during welding was

limited; however, it was seen that each weld type produced continuous layers of IMC's at the Al-Fe interface owed by the relatively flat nature of the interface. Al-Fe IMC's are innately brittle and susceptible to cracking, while a continuous layer of IMC's provides an easy path for cracks to propagate through. This was the reason why minimal growth of IMC's at the Al-Fe interface as reported by the authors showed a drastic reduction in weld tensile strength.^[12,16,18,30-35] On the other hand, VFAW generates a very heterogeneous microstructure with a wavy interface as seen in Figure 6. The IMC growth is not homogeneous across the entire weld interface. The wavy nature of the interface (mid-weld region) leads to isolation of the IMC's, separated from each other by the crests and troughs of the waves. The outer-weld region sees very less growth of IMC's even at high annealing temperatures as observed in Figure 8. This discontinuity in the IMC growth can arrest crack growth.

However, the microstructure of VFAW welds being inherently heterogeneous did result in large deviations of weld toughness values between tests within the same annealing conditions. This is observed by the weld toughness spread between the maximum and minimum values seen in Figure 7 as well as in Table III. This discrepancy is seen for the anneals at or below 500 °C as well as for the as-welded samples. Having a deviation in

weld fracture toughness of the as-welded samples is expected to carry out to the annealed samples. The mechanical properties of a weld are dependent on its microstructure and VFAW welds as explained earlier have very heterogeneous microstructures that can differ between welds. Another reason for the weld fracture toughness deviation of the annealed samples is that annealing VFAW welds produces uneven IMC growths across the weld interface that also differs between welds as illustrated in Figures 6 and 8. Welds that have regions of more discontinuous IMC growths post annealing will likely have greater fracture toughness than the welds that exhibit more uniform growth. This is because crack propagation as a result of an external stress will be hindered by regions of low IMC growth. Other welds that have more uniform IMC layer thickness across the weld interface should have poorer fracture toughness due to greater ease of crack propagation.

To ascertain the validity of the wedge test, SEM images were taken on the fracture surface of a steel sheet peeled apart from the Al sheet upon wedge testing. Figure 9 presents results from a wedge test performed for an as-welded sample with no post-weld heat treatment. The steel side fracture surfaces (both SE and BSE images) showed depth, phase contrast and mixed compositions of Fe and Al, indicating desirable interfacial failure. In the case where the interface was stronger than the base metal, the limiting value, which is the wedge toughness of the aluminum would be reached. Such a test would show a planar uniaxial scratched surface revealing only one phase with a composition mainly composed of Al as a result of the wedge drifting and cutting into the Al sheet during a test. Generally, as the weld strength increases, the chance of wedge cutting increases. Most tests including the as-welded samples did successfully peel without wedge cutting. However, the 300 °C annealed samples with no IMC growth nearly always cut.

B. Thermal Exposure: Effect on Interface Structure

Figure 6(a) presents a schematic of a typical impact welded interface showing the locally varying structure. Various locations of the welded interface are marked in the bottom of Figure 6(a). It can be observed from

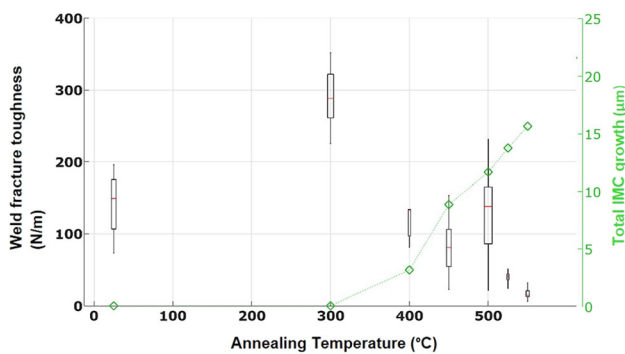


Fig. 7—Weld strength and IMC growth as a function of annealing temperature.

Table III. Reports Weld Toughness Data Collected From Wedge-Tested VFAW Welds With Different Annealing Conditions

Annealing Temperature (°C)	IMC Growth (μm)	# of Tests	Failure Mode		Weld Fracture Toughness (N/mm)		
			Weld Interfacial Failure	Base Material Cutting	maximum	minimum	mean
None	0	10	yes	no	196	73	142
300	<< 3	13	no	yes	352	151	282
400	3.1	5	yes	no	198	81	129
450	8.8	10	yes	no	153	22	83
500	11.6	17	yes	no	231	21	122
525	13.7	4	yes	No	51	24	39
550	15.6	7	yes	no	32	6	17

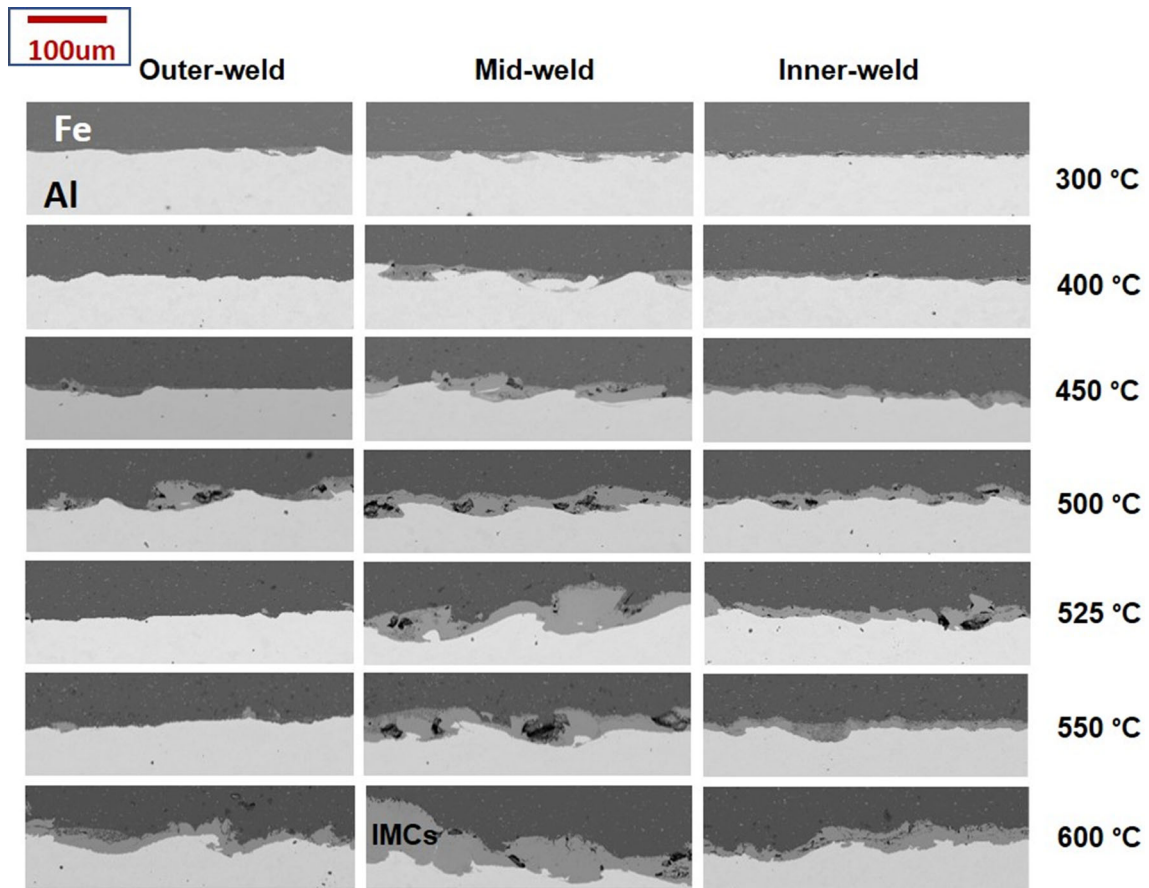


Fig. 8—SEM BSE images of Al-Fe VFAW welds annealed at different temperatures.

Figure 6(a) that based on the distance from the weld center, the interface morphology varies. This can be attributed to the variation in the two key parameters in developing an impact weld, the local impact velocity and angle. Note that the impact velocity mentioned here is the velocity at which the flyer impacts the target, which is different from the collision point velocity.^[2] Impact velocity is dependent on a number of factors including the material properties like strength and thickness, welding parameters like standoff distance and the way the standoff is created, foil geometry, and input energy, whereas impact angle mostly depends on the standoff distance. Impact welding of metals ideally occurs when these two welding parameters fall within an optimum range. Although the range varies depending on the material pair, metallurgical bonds have been typically observed at velocities ranging between 300 and 1000 m/s and angles between 5 and 20 deg.^[2,46–48] Previous VFAW studies with aluminum (1XXX/2XXX/6XXX series) as the flyer material with thicknesses ranging between 0.5 and 2 mm, input energies between 6 and 8 kJ, and standoffs of 1.6 and 2.5 mm have recorded impact velocities between 650 to 900 m/s with successful metallurgical bonding.^[4,41,49–54] As the weld progresses the impact angle increases continuously, whereas the impact velocity decreases from a maximum at the inner edge of contact at the boundary of the unwelded zone to

a minimum at the outer edge of contact, where there is no weld. This has been schematically depicted in the top of Figure 6(a). Note that impact velocity and angle measurements have not been performed in this study and as such the curves presented in Figure 6(a) are only representative and may not depict the actual shape; however, the trends are represented correctly. The distance and velocity numbers marked on the plot are also representative. The angle θ_{max} represented in Figure 6(a) is the maximum impact angle between the flyer and target in a region of no welding. This value was measured from a welded sample using ImageJ software and is approximately 44 deg.

Figure 6(b) shows SEM BSE images taken from different regions *i.e.*, “Outer-weld”, “Mid-weld”, and “Inner-weld” of an as-welded VFAW sample. As depicted in Figures 6(a) and (b), the interface morphology changes across the span of an Al-Fe VFAW weld in the as-welded condition. The center or unwelded region between the top and bottom welds is the result of the zero angle of impact between the flyer and target sheets.^[55] Although, VFAW an impact welding technique falls under the realm of solid-state welding technology, evidence of localized melting has been found both experimentally and through numerical simulations.^[49,56–60] Based on the combination of the impact velocity and angle, temperatures above melting

point of joining members can be reached locally, leading to localized melting. Similar results have been observed in this study. The outer-weld region is relatively flat with minimal atomic mixing and melting at the interface. In the outer-weld section, the impact angle is greater while the impact velocity is lower producing a metallic bond with less interface alteration and melting.^[55] The mid-weld region has the greatest wavelike character with non-continuous melt zones. The inner-weld section has less wavelike character with more continuous melting and atomic mixing. Moving towards inner-weld region, the impact angle decreases while the impact velocity increases. This causes an increase in heat release from the impact and deformation at the weld interface. Near the center region where the impact angle is lowest, and the impact velocity is highest, the interface loses wavelike character due to more excessive melting. The degree of melting controls the growth of an Al-Fe IMC layer at the weld interface which is most observed in the inner-weld.

Figure 8 depicts micrographs taken from these three different regions for VFAW welds annealed at different temperatures ranging from 300 °C to 600 °C. As illustrated in Figure 7, a clear trend is shown where the IMC thickness increases as the annealing temperature goes up for the mid-weld and inner-weld regions. However, for modest anneals at 300 °C, there is little to no growth of IMC's in all the three weld regions. There is no clear trend with annealing temperature on the outer-weld. In fact, for the outer-weld, IMC growth is observed to be less at 525 °C and 550 °C as compared to 500 °C. As mentioned earlier, welding using VFAW produces a very heterogeneous microstructure at the

weld interface that shows a varying degree of plasticity and random distribution of melt zones which increase towards the inner-weld. This complexity will produce some differences in microstructures even between welds that use the same setup and welding parameters. The outer-weld region has very little to no melting and nucleation of IMC due to a combination of suitable impact parameters *i.e.*, lower impact velocities and higher impact angles. Melt regions in Al-Fe weld produces IMC phases that act as nucleation sites for easy IMC growth during an anneal. Without the presence of IMC, nucleation of these compounds must occur before growth. When there is great bonding and existing IMC, the growth of further IMC is easy, whereas if it is missing there does seem to be a significant barrier to IMC growth. This can represent an opportunity to make quasi-stable interfaces by not forming IMC's from the start. The two VFAW samples annealed at 525 °C and 550 °C lacked IMC phases on the outer-weld in the as-welded condition. Therefore, nucleation of these phases was required first which did not happen because the activation energy to trigger this process was not satisfied during the time span of the anneals. The IMC growth is significantly greater in the mid-weld as compared with the other regions especially at the annealing temperatures of 500 °C and higher. The main reason for this is that the impact angle and speed in the mid-weld region is optimal to maximize the metallurgical bond between the alloys. A strong metallurgical bond maximizes the ease of atomic diffusion across the interface promoting faster IMC growth. Also, the interface in this region is significantly wavier compared with the other regions increasing the interface area for

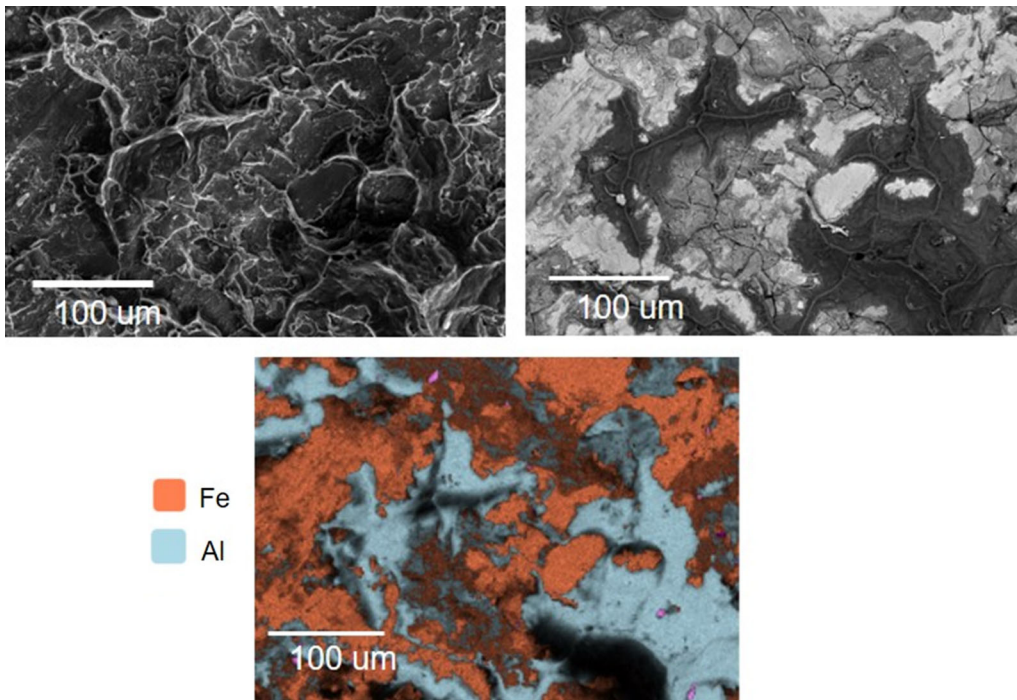


Fig. 9—SE image (top left), BSE image (top right), and an EDS map (bottom) of the steel side fracture surface of the Al-Fe VFAW weld produced from wedge testing.

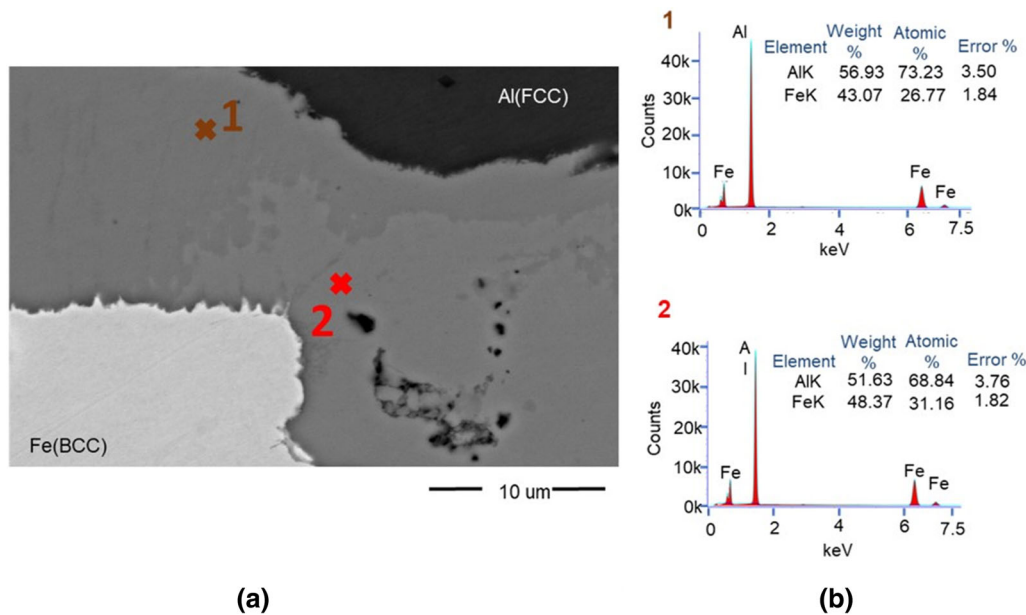


Fig. 10—(a) SEM BSE image focused on the weld zone of a VFAW weld heat treated at 525 °C for 140 min and (b) results of the EDS point scans.

diffusion during annealing. EDS point analysis (Figure 10) conducted on the melt region of a VFAW weld annealed at 525 °C confirmed the presence of two different IMC's, FeAl_3 and Fe_2Al_5 , found between the Al-FCC and Fe-BCC phase bands, which agrees with the results presented in literature.^[1,3,16,18,19] Figure 10(a) shows an SEM BSE image with marked regions identifying the location of each EDS point scan. The EDS results along with the compositions of each identified element are displayed in Figure 10(b).

C. Simulation

A plot of total IMC layer growth with annealing temperature varying in δ is illustrated in Figure 11(a). This IMC growth refers to the growth of IMC's during the anneals excluding IMC formation during the welding process. The three dotted red curves in Figure 11(a) are calculated results using δ of 0.25, 0.50 and 0.75 nm. Figure 11(b) illustrates the simulation results of total Al-Fe IMC growth carried out using different g_d^0 of the IMC's. This is captured in the top four curves which use g_d^0 of the IMC's ranging from 10 nm to 200 nm using a constant δ of 0.25 nm. In both the Figures 11(a) and (b), the green dotted curves represent the simulation results excluding short circuit diffusion and the black markers represent the experimental results from this work. IMC growth reported by three external sources^[3,21,61] are also provided in Figures 11(a) and (b). Each source provided, fit curves in their reported IMC growths with respect to annealing time at various fixed annealing temperatures. As shown in Figures 11(a) and (b), the IMC growths were calculated at the annealing time in this study and plotted from the equations of each fit curve. Movahedi *et al.*^[3] measured the IMC growth at the interface of friction stir welds,^[3] while Kajihara

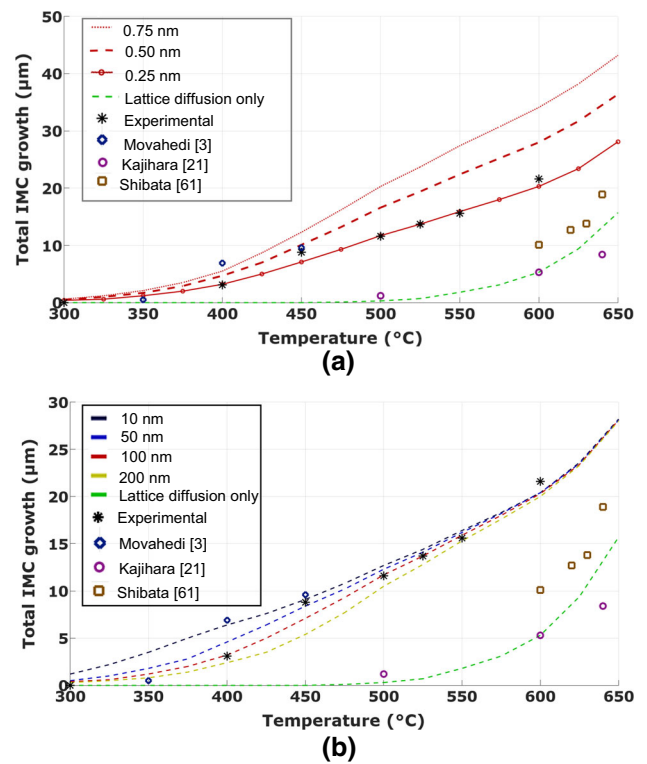


Fig. 11—(a) variation of simulated and experimental data following this study and other works of IMC thickness gains with respect to annealing temperatures for (a) varying δ and (b) varying g_d^0 of the IMC's.

et al.^[21] and Shibata *et al.*^[61] measured the IMC growth of Fe_2Al_5 from diffusion couples.

The choice of initial grains sizes in the Al (FCC) and Al-Fe BCC phases was set at 0.1 and 2 μm, respectively, in both Figures 11(a) and (b). Simulations were first

carried out by applying the lattice diffusion profiles of the Al-Fe system as illustrated in Figure 4(b) and Table I. The results showed nearly no IMC growth below 500 °C with very modest growths between 500 °C and 600 °C. These calculated IMC growths for the reported span of annealing temperatures are well below the experimentally determined IMC growths illustrated by the black markers on Figures 11(a) and (b). This observed discrepancy between the calculated and experimental results suggests that short circuit diffusion is a major contributor to IMC growth of VFAW welds and should be incorporated into the simulation to properly represent the outcome of annealing VFAW welds. There are few factors not addressed in the simulation that has the potential to heighten the lattice diffusivity leading to greater IMC growth than predicted. The first is the energy produced from significant plastic deformation of grains near the interface of a VFAW weld. This energy can provide a driving force for phase transformation at the interface promoting greater IMC formation rates. The deformation at the weld interface also leads to the formation of point defects providing sites for atomic movement enhancing lattice diffusivity. Lastly the composition of the Al_xFe_y may deviate slightly from perfect stoichiometry promoting the formation of constitutional/anti-site defects enhancing the lattice diffusivity.

It is observed that the calculated IMC growths using lattice diffusion only is in better agreement to the IMC growth of References [21, 61]. The likely reason for this is that the diffusion couples are made by heat treating sandwiched pieces of Al and Fe to establish a diffusion bond. The interface should have minimal deformation during this process which means that lattice or volume diffusion should be the limiting step of IMC grain growth.

The remaining non-green dashed curves in Figures 11(a) and (b) are the results of including grain boundary diffusion kinetics to the simulations. As shown in Figure 11(a), the less known input variable δ for the simulations was varied to capture three different trends (red dashed curves) of IMC growth with annealing temperature. The lack of knowledge of δ is due to the lack of experimental work conducted to measure this term, arising from the difficulty and complexity of measuring this in metals.^[29] Assumptions were made for setting the initial grain sizes of each phase used in the simulations. The reason for this is that the phases at the as-welded VFAW weld interface could not be experimentally determined since the microstructure in that region is too heterogeneous. The heterogeneity comes from nucleation of new grains in the melt zones and numerous regions of recrystallized grains. Since IMC phases formed heterogeneously across the weld interface occur during the rapid VFAW welding process, it is expected that these grains are mostly submicron in size. The reason for this is that these grains are formed from nucleation at the weld interface with minimal chance to grow. Also, regions at the weld interface lacking intermetallic phases must nucleate before growth, lowering the overall average initial grain sizes of the IMC's prior to annealing. Al-FCC phase is expected to have an average grain size in the submicron range due to the

phase having greater susceptibility to deformation and recrystallization, while the Al-Fe BCC phase should have larger grains. As explained in Section II-E, the choice of initial grain sizes in the solid-solution phases is not as critical to the growth of IMC during annealing. The plot in Figure 11(a) shows that the experimental results have consistently lower IMC growths than the simulated results when the two higher δ values were used. As explained earlier in Section III-A, nucleation for parts of the weld can be a rate limiting step for IMC growth. If parts of a weld do not grow any IMC's due to sluggish nucleation, the average IMC growth of the whole weld will be slower. Therefore, this can be one of the reasons why the IMC growth experimentally measured is lower than the computational results. Meanwhile, the computational results could be more reliable if grain boundary diffusion in the Al-rich intermetallic phases was experimentally known. Another thing to note is that the experimental results shows a Arrhenius type relationship of the IMC growth with annealing temperature. The growth of IMC's is, however, sensitive to the initial grain size in the IMC's. The simulations were therefore carried out by varying the initial grain size of the IMC's from 10 to 200 nm. δ was set at 0.25 nm following the best fit with the experimental data seen in Figure 11(a). The results of these simulations is illustrated in Figure 11(b), which shows that the slope of IMC growth with temperature becomes steeper with greater initial IMC grain size. Figure 11(b) also shows that when an initial IMC grain size of 100 nm is applied to the simulations, the IMC's growth trend with temperature best matches with the trend in the experimental results. This means that it is likely that the average initial grain size of the IMC's at the interface of each as-welded VFAW weld is close to 100 nm. However, this can only be speculated since no experimental work was conducted to measure the grain size of the IMC's.

IV. CONCLUSIONS

The present study investigated the effect of annealing on the structure and properties of Al-Fe impact welds made using VFAW. Trends between processing, microstructural evolution, and mechanical properties of annealed Al-Fe VFAW weld couples were captured. This study reached the following conclusions:

1. An existing method of measuring local toughness *via* wedge testing was adopted to measure fracture toughness in aluminum steel lap welds.
2. Small thermal exposure increases toughness, possibly due to healing by means of sintering voids at the weld interface without growth of intermetallics. Higher temperature exposure forms continuous IMCs causing toughness to degrade dramatically.
3. Intermetallic formation is far too fast to be predicted by lattice diffusion. The IMCs that form must have very high defect structure that aids diffusion and to effectively model the behavior, coarsening of the highly dislocated structure created

must be considered. Initial intermetallics provide nuclei that speed the process of forming IMCs.

4. Due to heterogeneity of the impact welded interface, the intermetallic growth contains discontinuous interface regions without IMCs which aids in arresting crack growth. An increase in the annealing temperature yielded an increase in IMC growth on the center and inside portions on the weld interface. However, on the outside portions where there was little initial IMC, new IMC formation was often delayed. This is presumably due to lack of nucleation sites.

ACKNOWLEDGMENTS

We gratefully acknowledge financial support from the National science foundation (NSF) under grant opportunities for Academic Liaison with Industry (GOALI), Award No. 1538736 and NSF Major Research Instrument Grant 1531785. The authors would also like to thank Center for Electron Microscopy and Analysis (CEMAS) at The Ohio State University for providing access to research facilities.

DISCLOSURE

No potential conflict of interest was reported by the authors.

REFERENCES

1. L. Xu, L. Wang, Y.C. Chen, J.D. Robson, and P.B. Prangnell: *Metall. Mater. Trans. A*, 2016, vol. 47A, pp. 334–46.
2. A. Kapil and A. Sharma: *J. Clean. Prod.*, 2015, vol. 100, pp. 35–58.
3. M. Movahedi, A.H. Kokabi, S.M.S. Reihani, H. Najafi, S.A. Farzadfar, W.J. Cheng, and C.J. Wang: *Mater. Charact.*, 2014, vol. 90, pp. 121–26.
4. S.R. Hansen, A. Vivek, and G.S. Daehn: *J. Manuf. Sci. E*, 2015, vol. 137, p. 051013.
5. P. Corigliano, V. Crupi, E. Guglielmino, and A.M. Sili: *Mar. Struct.*, 2018, vol. 57, pp. 207–18.
6. J. Conklin, R. Beals, and Z. Brown: *SAE Tech. Pap.* (No. 2015-01-0408), (2015).
7. K. Smith and Y. Zhan: *SAE Tech. Pap.* (No. 2015-01-0410), (2015).
8. H. Springer, A. Kostka, E.J. Payton, D. Raabe, A. Kaysser-Pyzalla, and G. Eggeler: *Acta Mater.*, 2011, vol. 59, pp. 1586–1600.
9. R. Qiu, C. Iwamoto, and S. Satonaka: *Mater. Design*, 2009, vol. 30, pp. 3686–89.
10. Y. Abe, T. Kato, and K. Mori: *J. Mater. Process. Tech.*, 2009, vol. 209, pp. 3914–22.
11. R. Qiu, C. Iwamoto, and S. Satonaka: *J. Mater. Process. Tech.*, 2009, vol. 209, pp. 4186–93.
12. R. Qiu, C. Iwamoto, and S. Satonaka: *Mater. Charact.*, 2009, vol. 60, pp. 156–59.
13. W. Cai, G. Daehn, A. Vivek, J. Li, H. Khan, R.S. Mishra, and M. Komarasamy: *J. Manuf. Sci. E-T ASME*, 2019, vol. 141.
14. M. Pouranvari and S.P.H. Marashi: *Sci. Technol. Weld. Joi.*, 2013, vol. 18, pp. 361–403.
15. B.P. Thurston, A. Vivek, B.S. Nirudhoddi, and G.S. Daehn: *MRS Bull.*, 2019, vol. 44, pp. 637–42.
16. R. Hatano, T. Ogura, T. Matsuda, T. Sano, and A. Hirose: *Mater. Sci. Eng. A*, 2018, vol. 735, pp. 361–66.
17. M. Honaripisheh, M. Asemabadi, and M. Sedighi: *Mater. Design*, 2012, vol. 37, pp. 122–27.
18. H. Springer, A. Kostka, J.F. dos Santos, and D. Raabe: *Mater. Sci. Eng. A*, 2011, vol. 528, pp. 4630–42.
19. L. Xu, J.D. Robson, L. Wang, and P.B. Prangnell: *Metall. Mater. Trans. A*, 2018, vol. 49A, pp. 515–26.
20. A.C.K. So and Y.C. Chan: In *1996 Proceedings 46th Electronic Components and Technology Conference*, 1996, pp. 1164–71.
21. M. Kajihara: *Mater. Trans.*, 2006, vol. 47, pp. 1480–84.
22. H. Springer, A. Szczepaniak, and D. Raabe: *Acta Mater.*, 2015, vol. 96, pp. 203–11.
23. M. Yilmaz, M. Cöl, and M. Acet: *Mater. Charact.*, 2002, vol. 49, pp. 421–29.
24. A. Kobayashi, M. Machida, S. Hukaya, and M. Suzuki: *JSM E Int. J. A*, 2003, vol. 46, pp. 452–59.
25. K. Mechsner and H. Klock: *Aluminium*, 1983, vol. 59, pp. 850–54.
26. D.R.G. Achar, J. Ruge, and S. Sundaresan: *Aluminium*, 1980, vol. 56, pp. 220–23.
27. L. Agudo, D. Eyidi, C.H. Schmaranzer, E. Arenholz, N. Jank, J. Bruckner, and A.R. Pyzalla: *J. Mater. Sci.*, 2007, vol. 42, pp. 4205–14.
28. G. Zhang, M. Chen, Y. Shi, J. Huang, and F. Yang: *RSC Adv.*, 2017, vol. 7, pp. 37797–805.
29. H.C. Akuezue and D.P. Whittle: *Met. Sci. J.*, 1983, vol. 17, pp. 27–31.
30. K. Miyamoto, S. Nakagawa, C. Sugi, H. Sakurai, and A. Hirose: *SAE Int. J. Mater. Manuf.*, 2009, vol. 2, pp. 58–67.
31. N. Chen, M. Wang, H.-P. Wang, Z. Wan, and B.E. Carlson: *J. Manuf. Process.*, 2018, vol. 34, pp. 424–34.
32. T. Tanaka, T. Morishige, and T. Hirata: *Scr. Mater.*, 2009, vol. 61, pp. 756–59.
33. M. Movahedi, A.H. Kokabi, S.S. Reihani, W.J. Cheng, and C.J. Wang: *Mater. Design*, 2013, vol. 44, pp. 487–92.
34. W.H. Jiang and R. Kovacevic: *P. I. Mech. Eng. B*, 2004, vol. 218, pp. 1323–31.
35. S. Yang, J. Zhang, J. Lian, and Y. Lei: *Mater. Design*, 2013, vol. 49, pp. 602–12.
36. N.R. Philips, M.Y. He, and A.G. Eva: *Acta Mater.*, 2008, vol. 56, pp. 4593–600.
37. E. Bruhwiler and F.H. Wittmann: *Eng. Fract. Mech.*, 1990, vol. 35, pp. 117–25.
38. Z. Chen, Q. Zhang, and J.C. Zhao: *J. Open Res. Softw.*, 2019, vol. 7.
39. G. Neumann and C. Tuijn: *Self-diffusion and impurity diffusion in pure metals: handbook of experimental data*, 2011, vol. 14.
40. G.E. Murch and C.M. Bruff: Springer, Berlin, 1990, pp. 340–52.
41. B. Liu, A. Vivek, M. Presley, and G.S. Daehn: *Metall. Mater. Trans. A*, 2018, vol. 49A, pp. 899–907.
42. C. Herzig and Y. Mishin: Springer, Berlin, 2005, pp. 337–66.
43. http://shodhganga.inflibnet.ac.in/jspui/bitstream/10603/77141/12/12_chapter_pct204.pdf, website accessed 11/2018.
44. C. Herzig and S. Divinski: *Diffusion Processes in Advanced Technological Materials*, Springer, Berlin, 2005, pp. 173–238.
45. H. Mehrer: *Diffusion Foundations Trans Tech Publ*, 2014, vol. 2, pp. 1–72.
46. A. Vivek, S.R. Hansen, B.C. Liu, and G.S. Daehn: *J. Mater. Process. Tech.*, 2013, vol. 213, pp. 2304–11.
47. A. Vivek, B.C. Liu, S.R. Hansen, and G.S. Daehn: *J. Mater. Process. Tech.*, 2014, vol. 214, pp. 1583–89.
48. B.C. Liu: Doctoral dissertation, The Ohio State University, 2016.
49. A. Nassiri, G. Chini, A. Vivek, G. Daehn, and B. Kinsey: *Mater. Design*, 2015, vol. 88, pp. 345–58.
50. J.T. Benzinger, M. He, A. Vivek, G.A. Taber, M.J. Mills, and G.S. Daehn: *J. Mater. Eng. Perform.*, 2017, vol. 26, pp. 1229–35.
51. T. Lee, S. Zhang, A. Vivek, B. Kinsey, and G. Daehn: *J. Manuf. Sci. E-T ASME*, 2018, vol. 140.
52. A. Vivek, S.R. Hansen, and G.S. Daehn: *Rev. Sci. Instrum.*, 2014, vol. 85, p. 075101.
53. A. Vivek, B. Liu, D. Sakkinen, M. Harris, and G. Daehn: *SAE Tech. Pap.* (No. 2015-01-0701), 2015.
54. B. Liu, A. Vivek, and G.S. Daehn: *J. Manuf. Process.*, 2017, vol. 30, pp. 75–82.

55. A. Vivek, S. Hansen, J. Benzing, M. He, and G. Daehn: *Metall. Mater. Trans. A*, 2015, vol. 46A, pp. 4548–58.
56. A. Nassiri, T. Abke, and G. Daehn: *Scr. Mater.*, 2019, vol. 168, pp. 61–66.
57. V. Gupta, T. Lee, A. Vivek, K.S. Choi, Y. Mao, X. Sun, and G. Daehn: *J. Mater. Process. Tech.*, 2019, vol. 264, pp. 107–18.
58. A. Nassiri, A. Vivek, T. Abke, B. Liu, T. Lee, and G. Daehn: *Appl. Phys. Lett.*, 2017, vol. 110, p. 231601.
59. R.N. Raelison, T. Sapanathan, E. Padayodi, N. Buiron, and M. Rachik: *J. Mech. Phys. Solids*, 2016, vol. 96, pp. 147–61.
60. A. Nassiri, S. Zhang, T. Abke, A. Vivek, B. Kinsey, and G. Daehn: In *Proceedings of the 3rd Pan American Materials Congress*, 2017, 83–93. Springer, Cham.
61. K. Shibata, S. Morozumi, and S. Koda: *J. Jpn. Inst. Met.*, 1966, vol. 30, p. 382.

Publisher's Note Springer Nature remains neutral with regard to jurisdictional claims in published maps and institutional affiliations.